ACS Sustainable Chemistry & Engineering

pubs.acs.org/journal/ascecg

Research Article

Insights into Sustainable Nitrogen Fixation by Gas-phase Spectroscopic Measurements and Global Modeling of Reaction Intermediates in Humid Nitrogen Plasma

Ananthanarasimhan Jayanarasimhan,[†] Robert Pierrard,[†] Sean M. Peyres, Shurik Yatom, Davide Curreli, and R. Mohan Sankaran*

Cite This: *ACS Sustainable Chem. Eng.* 2025, 13, 140−150

Read Online

ACCESS | Metrics & More | Article Recommendations | Supporting Information

ABSTRACT: There is growing interest in reacting molecular nitrogen and water to sustainably synthesize fixed forms of nitrogen such as ammonia. In particular, low-temperature plasmas can activate these relatively inert feedstocks at or near room temperature without a catalyst. However, because of the enhanced reactivity and nonequilibrium chemistry, a diverse range of products is formed, and the underlying reaction mechanisms are exceedingly complex. In this work, we studied a simplified reactor consisting of a gaseous plasma containing controlled mixtures of nitrogen gas and water vapor. Densities of key chemical species such as N, H, OH, NH, and NO were measured by emission and laser-based spectroscopy as a function of the relative humidity. A global model was constructed and the reaction network was validated by comparing calculated species densities with experiments. We discover that N, a key initial intermediate for ammonia, strongly decreases in the presence of water vapor, and as a result, ammonia formation becomes limited at high relative humidity. This decrease is surprisingly not because N itself reacts, but because one of its main sources, an excited molecular nitrogen state, is reacted away. In addition, oxidation pathways for nitrogen, which lead to NO and related products, are found to be favored over reduction pathways because the corresponding reverse reactions are less significant. Together, this understanding helps explain previously reported observations of selectivity toward nitrogen oxides over ammonia, particularly at higher relative humidities.

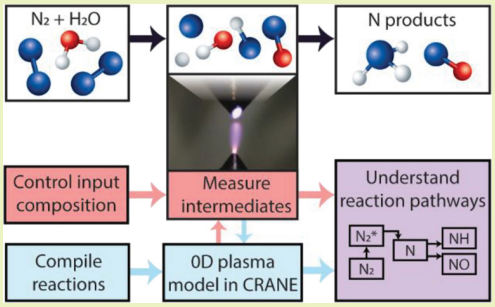

KEYWORDS: *nitrogen fixation, ammonia, plasma-liquid, atmospheric-pressure plasma, laser-induced fluorescence*

1. INTRODUCTION

The sustainable fixation of nitrogen is of growing interest to decarbonize and modularize the production of ammonia (NH_3).[1] Decarbonization can be achieved by modifying the current industrial Haber−Bosch (H−B) process and incorporating carbon capture (so-called "blue" ammonia) or providing the molecular hydrogen gas (H_2) feedstock via electrochemical splitting of water (so-called "green" ammonia).[2] While steps along these lines are relatively short-term and already underway, decentralization of NH_3 production requires moving away from H−B and is a much longer-term prospect. One of the visions for an alternative approach for NH_3 production is to directly react molecular nitrogen gas (N_2) and water (H_2O), which are both incredibly abundant and carbon-free. Unfortunately, both N_2 and water are relatively chemically inert and difficult to activate without going to very high temperatures, even higher than the reaction of N_2 and H_2 carried out by H−B.[3]

Plasmas are known to be capable of activating N_2 with their long history in nitrogen fixation[4] and ozone generation.[5] In addition, the reactivity can be generated without a catalyst or external heating. These properties have been recently applied to the reaction of N_2 and water. In particular, plasmas containing N_2 gas have been formed in contact with liquid H_2O, the two typical physical states of these reagents, and the formation of NH_3 has been demonstrated.[6−9] Plasmas have been generated both outside the liquid, as jets in a gas flow,[8,10,11] and inside the liquid, with bubbles to enhance gas breakdown.[12] Water has also been introduced in the gas phase as vapor[7,10,12−17] and liquid droplets (i.e., aerosol).[18]

Despite promising results, several issues remain to be addressed. The products are not limited to NH_3 or ammonium ions (NH_4^+) and include other fixed and oxidized forms of nitrogen even when N_2, rather than air, is used as the feed, including nitric oxide (NO) and nitrogen dioxide (NO_2), and nitrate (NO_3^-) and nitrite (NO_2^-) ions. Understanding of the physical and chemical processes that lead to the different

Received: July 13, 2024
Revised: November 19, 2024
Accepted: November 20, 2024
Published: December 18, 2024

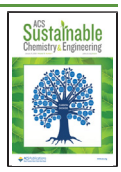

products has been challenged by the complex multiphase species transport and reaction.[19] Even in the case of plasmas that are formed outside liquid H_2O, the gas-phase chemistry involves not only activated N_2 species, but also activated H_2O species created by evaporation or sputtering.[20] Perhaps because most of the energetic species are contained in the plasma, there is evidence that much of the chemistry that controls the final products occurs in the gas phase.[8,21−23] A strong dependence of the fixed nitrogen product yields and distribution on H_2O vapor concentration has been reported by several groups.[7,10,16] A question has also been raised as to whether NH_3 is first formed in the gas phase and then dissolves to produce the detected NH_4^+, or if NH_4^+ is formed in the liquid phase.[8] However, very few studies have provided fundamental insight into the N_2−H_2O reactivity created by a plasma process. The potential importance of two intermediates, atomic nitrogen (N) and an electronically excited state of N_2, $N_2(A^3)$, on NH_3 formation has been spectroscopically revealed by Sakakura et al.,[15] and the dependence of NH_3 formation on water vapor concentration has been established by Bogaerts and co-workers.[8,10]

Here, we present a combined spectroscopic and modeling study of N_2−H_2O plasma chemistry. We set up a gaseous plasma and introduced controlled mixtures of N_2 and H_2O vapor similar to a previous study, but focused on the reaction chemistry inside the plasma as opposed to in the afterglow or further downstream.[10] Laser-induced fluorescence (LIF), two-photon absorption laser-induced fluorescence (TALIF), and optical emission spectroscopy (OES) with argon as an actinometer were applied to quantitatively measure several key reaction intermediates including N, H, OH, NH, and NO. A global model (i.e., zero-dimensional) was developed to calculate species densities and was validated by comparing the output with experiments. The model was then used to obtain insight into the mechanism and reaction pathways for species. Importantly, we find that N, produced from the dissociation of $N_2(A^3)$, is key to forming NH, which in turn is key to forming the final NH_3. As the H_2O vapor concentration increases, N decreases rapidly because $N_2(A^3)$ reacts more favorably with H_2, one of the byproducts of H_2O activation. In addition, N reacts with OH, another byproduct of H_2O activation, to generate NO_x products. While N continues to form NH, the reverse reaction of NH to form N limits its steady state concentration. As a result of these pathways, NH_3 production is limited, reaching a maximum at lower H_2O vapor concentrations, and then decreasing as the H_2O vapor concentration increases, which is consistent with several previous reports.[7,8,10] These findings provide detailed understanding of humid N_2 plasma chemistry and could guide future directions to improve and optimize sustainable fixation of N_2 by this approach.

2. METHODS

2.1. Plasma Reactor. To maintain a controlled gas-phase environment and enable spectroscopic measurements, a plasma reactor was set up consisting of a six-way stainless steel vacuum chamber with feedthroughs for gas lines and electrodes, and viewports for optical access. While experiments were carried out at atmospheric pressure, the vacuum chamber was found to be convenient for purging and introducing the different gas mixtures studied, and for providing a well-defined geometry to optically probe and collect light from the plasma.

The gas feed in our experiments was a mixture of N_2 and H_2O vapor. To introduce prescribed concentrations of H_2O vapor, there were two gas lines, one containing dry N_2 directly from a gas cylinder (Airgas, ultrahigh purity grade) and another containing wet N_2, made by bubbling the gas through liquid H_2O at room temperature to saturate the N_2 with H_2O vapor. The dry and wet N_2 were mixed at controlled ratios by using mass flow controllers (Alicat, MC Series). The final H_2O vapor concentration was confirmed by measuring in-line with a humidity probe (Omega RH-USB) and could be systematically varied between 5% and 90% relative humidity (RH). The total gas flow rate in all experiments was 400 sccm.

The plasma in this study was a direct current (DC) powered, glow-like discharge formed between two electrodes, which served as a surrogate for plasmas that have been previously reported for the conversion of N_2 and H_2O in a plasma-liquid setup.[6,23,24] While other plasma sources have also been studied, such as dielectric barrier discharges (DBDs), the filamentary nature would make it challenging for our diagnostics. Nonetheless, the properties of our DC plasma are close to a single filament within a DBD.[25] The electrodes consisted of 1/16" diameter and 1/8" diameter stainless steel cylinders with sharpened tips, serving as the cathode and anode, respectively. Electrodes were positioned by aligning the tips, which was found to stabilize the discharge, at a gap of less than 1 mm. The plasma was operated by connecting the anode to a high voltage positive power supply (Stanford Research Systems, Model PS350). A 500 kΩ ballast resistor in series with the power supply allowed the current to be controlled after igniting the plasma.

2.2. Optical Emission Spectroscopy and Actinometry. Optical emission spectroscopy (OES) was carried out by collecting plasma emission through a quartz window with an optical fiber coupler mounted to a two-axis translational stage. The position of the fiber was adjusted to maximize the emission intensity. As a result of the small length scale of the plasma (∼1 mm), the spacing between the plasma and the fiber, and the solid angle of detection of the fiber, radiation from the entire plasma was collected at once and the spectra represent an average of the plasma volume.

The fiber was coupled to a spectrometer (Princeton Instruments, Model HRS-500) with an 1800 g/mm diffraction grating and spectra were captured with a charge-coupled device (Princeton Instruments, PIXIS CCD), which provided a spectral range of approximately 200 to 850 nm. A calibrated deuterium/tungsten broadband light source (B&W Tek, BDS100) was used to account for the variable spectral response of the system. To estimate the densities of species by actinometry, argon gas (Ar) (Airgas, ultrahigh purity grade) was added to the gas feed up to a maximum concentration of 5%. In general, actinometry assumes that the excited states for both the species of interest and the reference gas (i.e., Ar) are populated only by electron impact from the ground state (Supporting Information, Figure S1). Using the excitation rates (Supporting Information, Figure S2) and quenching rates corresponding to these states, the measured emission intensities (Supporting Information, Figure S3) were converted to ground state densities. The transition probabilities and emission and quenching coefficients were obtained from the literature (Supporting Information, Tables S1 and S2). Additional details are included in Section S1 of the Supporting Information.

2.3. Laser-Induced and Two-photon Absorption Laser-Induced Fluorescence Measurements. LIF and TALIF were performed by focusing the output of a tunable laser system, consisting of a Nd:YAG laser pumping an optical parametric oscillator (OPO), onto the center of the plasma, corresponding to the positive column of the DC glow discharge. The excitation wavelengths for the target species, N, H, and OH, were 206.7, 205.1, and 282.6 nm, respectively, and the corresponding fluorescence were at 656, 742, and 310 nm, respectively.[26−29] A PiMax4 CCD was used to acquire the fluorescence signal. LIF measurements were calibrated by Rayleigh scattering measurements and by solving a four-level population kinetic model (Supporting Information, Figures S4−S6), whereas TALIF measurements were calibrated by using Kr as a reference gas (Supporting Information, Figure S7). Coefficients and parameters needed for the calculations were obtained from the literature (Supporting Information, Tables S3−S5). Additional details are included in Section S2 of the Supporting Information.

https://doi.org/10.1021/acssuschemeng.4c05771
ACS Sustainable Chem. Eng. 2025, 13, 140−150

2.4. Global Kinetic Modeling. A global chemical-kinetic reaction network was developed for modeling the humid N_2 plasma chemistry consisting of electron-impact reactions, including dissociation, attachment, ionization, recombination, and excitation; thermal reactions, involving heavy neutral particles and ions; and optical transitions. Overall, as summarized in Table 1, we considered a total of 338 reactions and 53 species, including 10 charged species. The reaction network was solved using CRANE,[30−32] an open-source chemical kinetic solver built on the MOOSE framework,[33] which can be used as a standalone solver. The rate constant or coefficient for each reaction was either calculated or obtained from the literature.[32,34−40] A detailed list of reactions and their corresponding rate constants can be found in Tables S6 of the Supporting Information. For some electron-impact reactions, cross sections from the literature were fed to LoKI-B, an electron Boltzmann equation solver, to calculate rate constants as a function of electron temperature (Supporting Information, Figure S8).[41] For other electron-impact reactions and thermal reactions, rate constant expressions as a function of electron temperature and gas temperature were found in the literature and are discussed in more detail in Section S3 of the Supporting Information. Additional details are included in Section S3 of the Supporting Information.

Table 1. Summary of General Types of Species and Reactions Considered in the Humid N_2 Plasma Chemical Reaction Network

species type	details	
neutrals	N_2, N, NH, NH_2, NH_3, NO, NO_2, NO_3, N_2O, H_2O, OH, HO_2, H_2O_2, O_2, O, O_3, HNO, HNO_2, HNO_3, H_2, H	
excited neutrals	N_2(v), N_2(A3, B3, C3, a'), H_2O(v), OH(A), O^1D, O^1S, H(n=2,3)	
charges species	N^+, N_2^+, N_4^+, OH^-, H_2O^+, H_3O^+, O^-, H_2^+, H^+, H^-	
reaction types	description of processes	no. of reactions
electron impact	excitation/deexcitation, ionization, recombination, dissociation, dissociative attachment/recombination	85
thermochemistry	quenching, excitation and ionization of N_2 electronic states	36
	other neutral-neutral	165
	ion- neutral reactions	20
	ion-ion reactions	21
optical transitions	radiative decay	11

2.5. Statistical Analysis. Experimental measurements were repeated whenever possible and the average and standard deviation of the data sets were calculated. Errors include both the contribution from the standard deviation and additional factors associated with data analysis. In the case of gas temperature measurements, there was error from spectral fitting. In the case of LIF/TALIF and actinometry measurements, there was error associated with the parameters used in calculating the absolute densities.

The presence of statistically significant differences between the mean values of experimental data was assessed by applying two sample *t* tests using the Minitab 2022 Statistical Software (Supporting Information, Table S7). A threshold value of $\alpha = 0.05$ was chosen, and a p-value at or less than 0.05 indicated significance. A summary of the *t* tests performed, and the resulting *p*-values are shown in Section S4 of the Supporting Information.

3. RESULTS AND DISCUSSION

We combined spectroscopic experiments, including OES and LIF/TALIF measurements, and modeling, based on global kinetics, to provide insight into nitrogen fixation occurring in a plasma containing N_2 and H_2O vapor. Figure 1a shows a schematic illustration of the experimental setup and the applied diagnostics. The close overlap of the experimental measurements and the modeling is shown by schematics of the respective process flows in Figure 1b. For example, OES provided basic plasma parameters such as the electron temperature and gas (neutral) temperature, which were used as inputs, along with the measured RH, for the model. The model was used to calculate densities of a wide range of species, including several key intermediates that were measured and compared for model validation. Compared species include N, H, and OH, which were measured by LIF/TALIF, and NH and NO which were measured by argon actinometry. The measured RH and electron and gas temperatures were

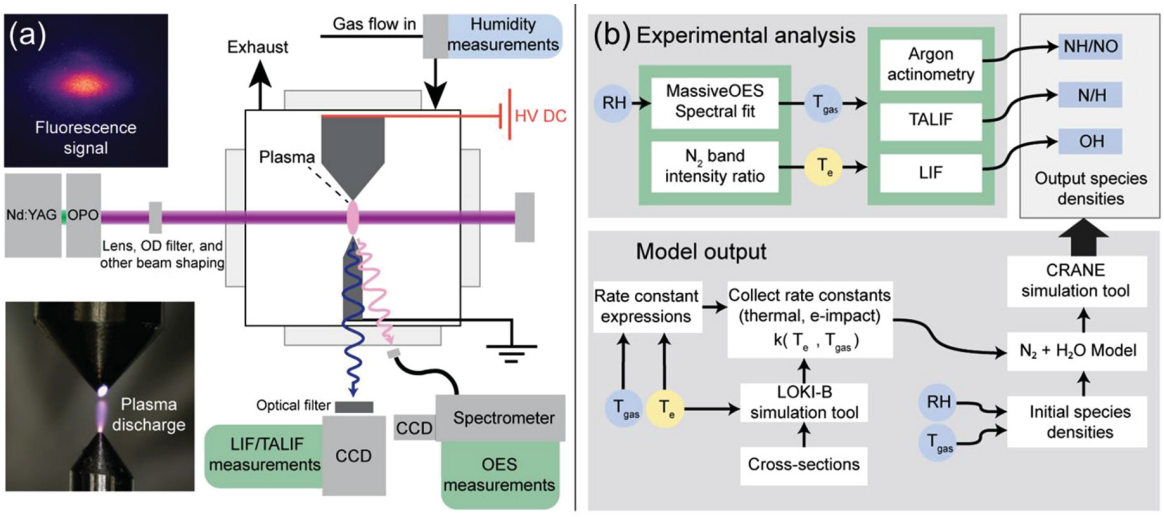

Figure 1. (a) Experimental schematic showing the setup for spectroscopic characterization of a humid N_2 atmospheric-pressure DC plasma. The RH was controlled by mixing a dry and wet N_2 gas flow stream and measured using a humidity probe. OES was carried out by collecting spectra from the entire plasma volume using a fiber optic coupled to a spectrometer. LIF/TALIF was conducted by directing a laser at the positive column of the plasma and collecting the fluorescence signal by a CCD. (b) Process flow for analysis of experimental measurements and model calculations. RH is an input condition for both experiments and modeling. Gas and electron temperatures were measured experimentally and then used as input conditions for solving the model and calibrating density measurements. Finally, measured and calculated densities were compared to validate the model. RH sensitive variables are shown in blue; the electron temperature was found to be RH insensitive and is shown in yellow.

https://doi.org/10.1021/acssuschemeng.4c05771
ACS Sustainable Chem. Eng. 2025, 13, 140−150

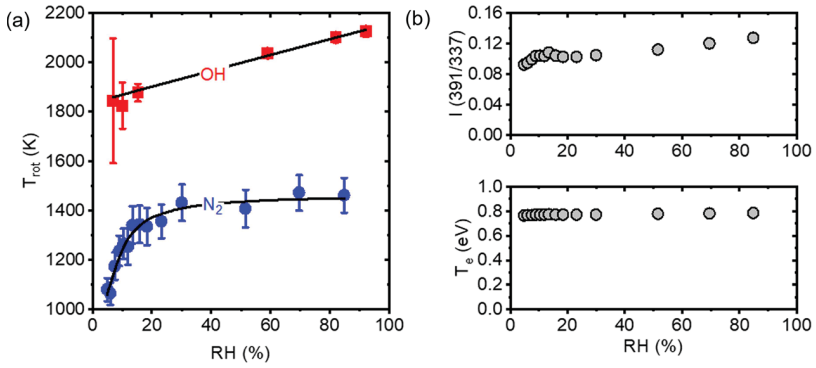

Figure 2. (a) Rotational temperatures obtained by spectroscopic analysis of N_2 rovibrational bands (blue circle), and OH rovibrational bands (red square) as a function of RH. Data points are an average of five measurements and error bars include contributions from both the standard deviation of the data and spectral fitting, with the latter being the main source of error. Solid lines are an empirical fit to the data (see eqs S18 and S19 in the Supporting Information). (b) Ratio of intensity of emissions lines at 391 and 337 nm (top figure) and corresponding electron temperatures, T_e, (bottom figure) estimated by modeling as a function of RH.

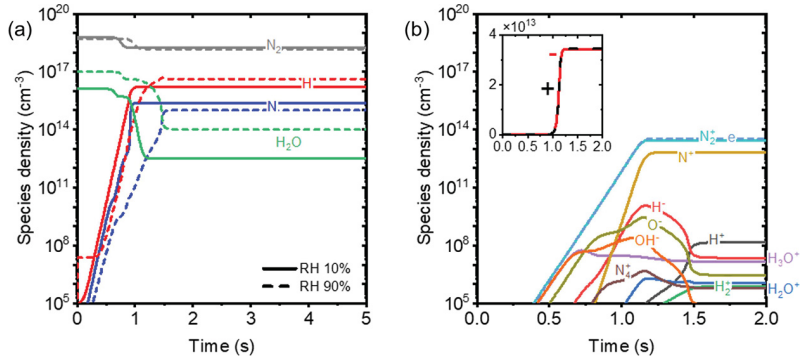

Figure 3. (a) Simulated temporal evolution of N_2, H_2O, N, and H densities at a RH of 10% and 90%. (b) Simulated temporal evolution of charged species densities at a RH of 90%. Inset shows the total density of positive ions (+) and negative ions (-), confirming quasineutrality.

additionally used in calculating the absolute species densities from LIF, TALIF, and actinometric measurements.

In the following sections, we will first discuss the basic properties of the plasma and evaluation of the model output. Then, we will show results for the species densities, measured by experiments and calculated by the model, as a function of RH. Finally, we will use our validated model to analyze mechanisms and reaction pathways to explain the formation of major fixed nitrogen products such as NH_3.

3.1. Gas and Electron Temperature. The gas temperature was obtained by the well-known method of fitting simulated spectra to the measured rovibrational spectra of molecular bands. In our case, two molecular emitting species were analyzed, N_2[42,43] and OH.[42−44] Figure 2a shows the rotational temperatures obtained from spectral fits to the N_2(C−B) and OH(A-X) bands as a function of RH (Supporting Information, Figure S9). We find that the rotational temperature associated with the N_2 rovibrational band increases at low RH before plateauing around 40% RH at ∼1400 K. In comparison, the rotational temperature associated with the OH rovibrational band increases linearly with RH and is higher than that of N_2. We also analyzed the spectra by the Boltzmann plot method (Supporting Information, Figure S10) and confirmed single rotational temperatures for N_2(C−B) and OH(A-X). The difference in the rotational temperatures between species may be the result of spatial effects; in particular, OH has been previously found to have locally varying densities in water vapor-containing plasmas.[45] Since N_2 is the predominant component, we assume that its measured properties best represent the average properties of the gas. The gas temperature was therefore assumed to be equivalent to the rotational temperature of the N_2(C−B) band based on the high collisionality at atmospheric pressure, which leads to rotational-translational equilibrium. Increasing gas temperature with RH has previously been reported and is linked to the vibration-to-translation (V-T) energy transfer rates.[46−48] Specifically, Ono et al. showed that the V-T time constant for $N_2(v = 1)$ decreases by approximately four to 5 orders of magnitude when the relaxation process shifts from N_2−N_2 collisions to N_2−H_2O collisions.[46] Vibrational temperatures were additionally obtained by spectral analysis of the N_2(C−B) and OH(A-X) bands and decrease with RH, consistent with an increased V-T energy transfer rate (Figure S11).

The measured dependence of the gas temperature on RH was fit to obtain an empirical expression that could be used to calculate the gas temperature at any RH (Supporting Information, Section S5). Although we measured two distinct rotational temperatures from the rovibrational fitting and analysis of the N_2 and OH bands, respectively, the former was used as the gas temperature input in the model since the plasma is mostly composed of N_2, and the latter was only used to calculate the Doppler broadening of the OH spectral line for LIF analysis.

The electron temperature was estimated based on a previously reported method of analyzing the intensity ratio of N_2 emission lines at 391 and 337 nm with the assumption

https://doi.org/10.1021/acssuschemeng.4c05771
ACS Sustainable Chem. Eng. 2025, 13, 140−150

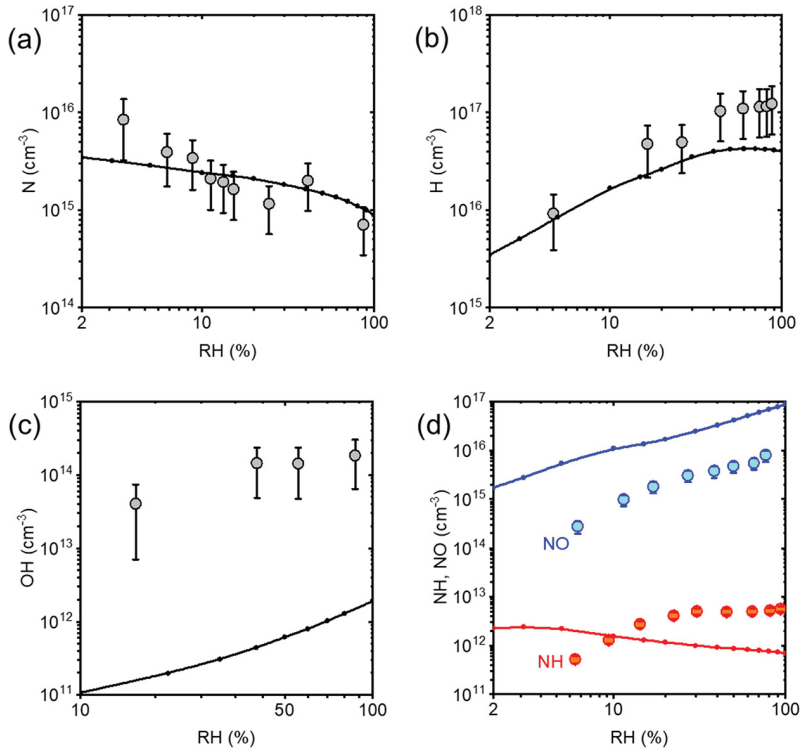

Figure 4. Density as a function of RH for (a) N, (b) H, (c) OH, (d) NH and NO species, experimentally measured by TALIF, TALIF, LIF, and OES, respectively (markers with error bars), and calculated by a global model (solid line with dots). Data points are the average of five measurements and error bars include contributions from both the standard deviation of the data and other sources. For TALIF and LIF, error includes parameters used to calculate the densities, including the gas temperature and background species densities. The solid line is a b-spline fit included as a guide for the model results.

that these states are populated only by electron impact reactions.[49,50] These lines correspond to the first negative system and second positive system band heads (v = 1), respectively. Here, we modified the analysis by simplifying our chemical reaction network (detailed in the next section) to only include the relevant reactions for N_2 involved in these emission lines (Supporting Information, Figure S12), and directly calculated the relative intensity of the emission lines as a function of electron temperature (Supporting Information, Figure S13). Additional details are included in Section S6 of Supporting Information. Figure 2b shows the intensity ratios of the N_2 lines at 391 and 337 nm measured by OES for our humid N_2 plasma as a function of RH, and the corresponding electron temperature, T_e, obtained by our analysis. We find that the intensity ratios, and to a greater degree T_e, are relatively constant across RH. For this reason, the electron temperature was assumed to be independent of RH and a value of 0.75 eV was chosen as an input for modeling.

3.2. Output of Global Chemical Kinetic Model. Following the development of a chemical reaction network for a humid N_2 plasma, our global (zero-dimensional) model outputs the densities of various plasma species, spatially averaged over an entire volume. We performed calculations with inputs from experimental measurements, including the electron temperature, gas temperatures, and RH's. The gas temperature dependence on RH was captured by an empirical expression, and the electron temperature was inferred from spectroscopic measurements, both explained in the previous section (Section 3.1).

Figure 3a shows calculation results for the temporal evolutions of a few representative neutral species, N_2, H_2O, N, and H, at two RH values. A steady state was achieved in all cases within a few seconds and the steady-state values were used for further analysis. In achieving a steady state, the densities of the initial reactant species (N_2 and H_2O) decrease with time as expected, reflecting the consumption of N_2 and H_2O to form products. Concomitantly, the densities of product species, including intermediates such as N and H, increase with time. The steady-state concentrations depend on the RH which will be discussed in more detail in the next section.

Figure 3b shows calculation results for the temporal evolutions of charged species at 90% RH. Again, a steady state was achieved in all cases over a few seconds. In the inset, the total densities of positively-charged and negatively-charged species are shown and found to be equal, confirming quasineutrality. We similarly checked that quasineutrality was achieved at all RH's studied. We note that the predominant negatively-charged species in our network are electrons, as expected, and the predominant positively-charged species are N_2^+ and N^+. A primary reason that the ionic species are mostly nitrogen is that the background gas is almost entirely made up of N_2 (~97.8−100% by volume for the range of RH studied). At higher RH, some ionic species from H_2O are observed including in order: H^+, which is formed from ionization of H; H^-, which is formed by dissociative attachment of electrons with H_2O; and H_3O^+, which is formed by reaction of H_2 and H_2O^+. Among the negative ions (OH^-, O^-, and H^-), H^- has the highest density because the rate constant for its formation by dissociative attachment (~10^{-19} m^3s^{-1}) is relatively larger than the rate for O^- (~10^{-20} m^3 s^{-1}) and OH^- (~10^{-22} m^3 s^{-1}). The conversion of H_2O^+ to H_3O^+ is consistent with

https://doi.org/10.1021/acssuschemeng.4c05771
ACS Sustainable Chem. Eng. 2025, 13, 140−150

observations by Keniley et al.[32] and Tropina et al.[51] and is the result of a fast charge transfer process.

3.3. LIF/TALIF/Actinometric Measurements and Model Calculations of Key Intermediates. A central focus of our study was the validation of the global model through comparison between its output and experimental measurement of key radical species. Both the experiments and modeling were carried out across RH values, and detailed statistical analysis is provided in Table S7 of the Supporting Information. In Figure 4a, TALIF measurements of N show a strong dependence on RH, with a sharp decrease in density with increasing RH. Model calculations reproduce the observed trend and absolute densities with good agreement at all RH values. TALIF measurements of H shown in Figure 4b also show a strong dependence on RH at lower RH, but with an increase in density with increasing RH. At higher RH values (≥40%), the H density does not increase significantly. Again, model calculations accurately reproduce the observed trend, but in this case, appear to underestimate the H density at higher RH values. In contrast, the density of OH measured by LIF (see Figure 4c) shows a smaller increase with RH. While this trend was reproduced by modeling, the difference in magnitude is much larger than in the case of N and H.

We also attempted to measure NH by LIF but we were unable to obtain a reliable signal, potentially because of the near resonant excitation-fluorescence at ∼336 nm and fast quenching.[52,53] Alternatively, the NH band at ∼336 nm corresponding to NH(A−X) was detectable by OES, and the NH density could be estimated by actinometry. The NH density shown in Figure 4d increases with RH before reaching a plateau at higher RH values (>20%). In comparison, model calculations show a small peak at lower RH, and a similar constant density at high RH. The actinometric measurements were extended to NO by measuring the band at ∼226 nm corresponding to NO(A-X). Figure 4d shows that the NO density increases with RH and is higher than NH throughout the range of RH's studied. The model calculations reproduce these trends, albeit with slightly higher densities.

The measured and calculated decrease in N density with increasing RH is likely because of the contribution of H_2O vapor to the N_2−H_2O plasma chemistry, rather than a physical change in the plasma properties since T_e (see Figure 2b), the electric field in the positive column (Supporting Information Figure S14), and the electron density (Supporting Information Figure S15) are found to remain relatively constant at different RH's from experimental measurements and model calculations. In comparison, the increase in H density with RH is relatively straightforward; with increasing H_2O vapor, there is a greater source of hydrogen. Nonetheless, we cannot exclude other chemical effects. For example, despite H_2O vapor making up only a maximum of 2.4% of the background gas at 100% RH, the measured and calculated H densities are always greater than the N densities. A similar H density trend with RH has been reported by Schröter et al. for humid argon plasmas at atmospheric pressure,[54] but with a much lower H density relative to the input H_2O concentration. On the other hand, the OH densities are substantially smaller than H, which is consistent with a similar report on a humid Ar plasma.[45] In light of the N density decreasing with increasing RH and the comparatively higher H density than OH, it is surprising that the NO density is higher than NH, but also consistent with a recent report.[10]

We note there are some discrepancies between experimental measurements and model results for a few of the species. In the case of NO and NH, actinometry relies on a quenching rate, and we found that the calculated absolute densities are sensitive to the quenching coefficients, which are not well-known (see Section S1 of the Supporting Information). Additionally, we assume that the reference, Ar, (as well as the target, NO or NH) is excited only through direct electron impact of the ground state, but at atmospheric pressure, the population distribution of excited Ar states has been shown to be out of equilibrium.[55] In the case of OH, the 0D model assumes a homogeneous plasma volume, but in actuality, the plasma is not spatially uniform. In particular, DC glow discharges are characterized by strong and asymmetric electric fields, which will lead to local variations in basic properties such as plasma density and electron temperature, as previously discussed (see Section 3.1). For example, electrons can be accelerated in the cathode sheath to very high energies, creating a population of hot electrons that deviate from a Maxwellian distribution. Such hot electrons may enhance direct electron impact reactions such as the dissociation of water vapor (see Section S7.2 of the Supporting Information). The inhomogeneous structure of the plasma may also lead to spatially varying species densities. These changes to the densities would have a particularly large impact on OH, since its density is relatively low compared to other species such as H. Future work is needed to include transport effects and extend the 0D model to 1D or 2D, in combination with spatially-resolved measurements of OH.

The noted differences between experiments and modeling primarily affect absolute densities, and some species, such as OH, more significantly than others. Nonetheless, our assumptions and simplifications are uniform across different RH's, and there is qualitatively good agreement in the trends of several species. With this validation of the model, we can extend the calculations and analysis to other species to provide further insight into the humid N_2 plasma chemistry.

3.4. Mechanism for Formation of Key Intermediates. One of the main goals of studying the reactivity between N_2 and H_2O is to develop a sustainable route to nitrogen fixation. The development of a plasma chemical kinetic model for humid N_2 that has been validated by experimental measurements of key intermediate species allows us to gain insight into potential mechanisms and reaction pathways.

Perhaps the most surprising observation is that with increasing RH, N decreases and H increases, but NH is relatively constant, indicating that N limits the formation of NH. To assimilate the many different reactions behind these trends, we analyzed the reaction rates. As shown in Figure 5a, the reactions that lead to the generation of N through vibrationally excited $N_2(v > 0)$ and electronically excited $N_2(A^3)$ state which are known to play a role in the splitting of N_2[39,56−58] are suppressed with increasing RH, especially $N_2(A^3)$ which becomes negligible. We find that the main reasons for this change are that $N_2(v > 0)$ is quenched by H_2O and $N_2(A^3)$ reacts more favorably with H_2, a product of H_2O activation, to form H and N_2 (R78 in Table S6 of the Supporting Information).[59]

At both low and high RH values, the main consumption reaction of N is its reaction with H to form NH. However, as noted, NH levels remain roughly constant (see Figure 4d). The reaction rate analysis of NH in Figure 5b shows that at both low and high RH values, NH reacts with H to reversibly form

https://doi.org/10.1021/acssuschemeng.4c05771
ACS Sustainable Chem. Eng. 2025, 13, 140−150

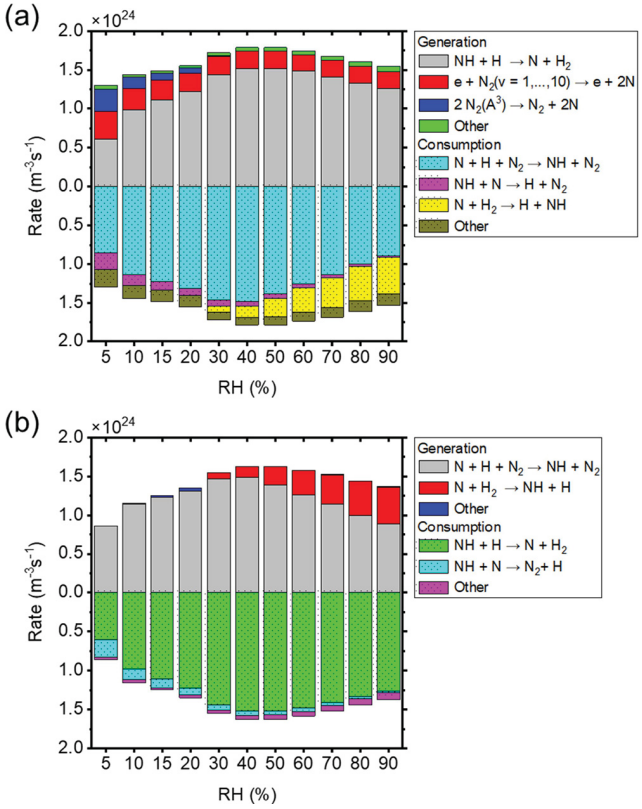

Figure 5. Reaction rate analysis showing dominant generation and consuming reactions for (a) N and (b) NH as a function of RH. All reactions that are shown individually contribute >5%, and "other" refers to the sum of all other reactions.

N, which has a much higher rate than the continued reaction to form NH_2. These reactions, in addition to the low densities of N at high RH and H at low RH, lead to the overall limited generation of NH.

Our identification of the potential role of N and $N_2(A^3)$ in the formation of NH and ultimately NH_3 is consistent with previous reports. Sakakura et al. detected N and $N_2(A^3)$ by absorbance and cavity ring-down spectroscopy of a dielectric barrier discharge plasma jet contacting liquid H_2O.[15] Bogaerts et al. detected $N_2(C_3)$, another electronically excited state of N_2, and NH in the spatial afterglow of a pulsed spark plasma jet by OES, and showed a correlation between their emission intensities.[8] In both cases, it was speculated that these species and their reactivity explain observed trends in the formation of NH_3, as well as NO_x. In the next section, we further analyze our model results to reveal the underlying pathways that lead to NH_3 and NO_x.

3.5. Reaction Pathways for Fixed Nitrogen Products.

Ultimately, the formation of NH_3, perhaps the most important fixed nitrogen product, starts with N and proceeds through NH. The key reaction paths that lead to the formation of NH_3 are illustrated as a process flow schematic in Figure 6. At low RH, N_2 is initially excited by electrons to either $N_2(A^3)$ or $N_2(v > 0)$, which react further with N_2 or electrons, respectively, to generate N. N subsequently reacts with H to first form NH, and then through sequential H additions forms NH_3. The formation of NH_3 is limited by the reverse reaction of NH to form N, and the relatively low rates for NH to NH_2 and NH_2 to NH_3. As described above, as the RH increases, N decreases and NH is limited despite the increased amount of H from H_2O vapor. There are additional effects of the increase in H. The recombination of H leads to the formation of H_2,

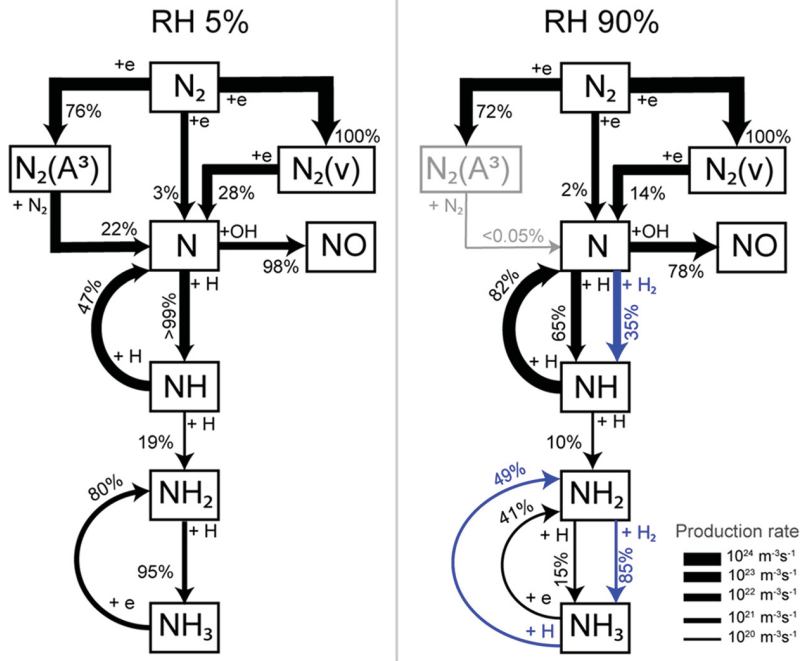

Figure 6. Schematic illustration of mechanisms and reaction pathways for NH_3 and NO production at a RH of 5 and 90%. Blue colored arrows and text indicate reaction channels that are absent at 5%, but opened at 90% RH. Gray colored arrows and text show reaction channels that are active at 5% and deactivated at 90% RH. The thickness of the arrows corresponds to the rate of the reactions specified in the legend. Percent values correspond to the fraction of the species produced from a given reactant. For simplicity, only the dominant reaction channels (1 to 3), summing to >90% of the total production are shown.

https://doi.org/10.1021/acssuschemeng.4c05771
ACS Sustainable Chem. Eng. 2025, 13, 140−150

which along with H itself, promotes the continued reactions of NH to NH_2, and NH_2 to NH_3. At the same time, H is also responsible for the reverse reactions of NH_2 to NH and NH_3 to NH_2. The competition between these different pathways can explain the trend we observe for the NH_3 density as a function of RH.

Another important fixed nitrogen product is NO_x (NO and NO_2). As shown in Figure 6, N reacts with OH to form NO at low and high RH. This reaction is referred to as the extended Zeldovich mechanism, which is a modified version of the Zeldovich mechanism that describes the formation of NO by reactions between N_2 and O_2 through either N or atomic oxygen (O). The extended Zeldovich mechanism has previously been reported in humid N_2[10] and humid air plasmas.[10,16] NO can further react to form N_2O and HNO_2 as well, by reaction with NH or OH, respectively.

While both H and OH increase in density with increasing RH, as they are byproducts of H_2O chemistry, the density of H is much higher than OH across RH (see Figure 4b,c). In terms of the rate constants, N is more reactive with H than OH (Supporting Information, Figure S16). It is thus surprising that our model calculations show the NO density is substantially higher than that of NH and related species (i.e., NH_2, NH_3). However, in comparing the reaction mechanisms for NH and NO described above and illustrated in Figure 6, there are key differences. The reduction pathway involves multiple reaction steps before yielding a stable species, whereas the oxidation pathway only requires one reaction step before a stable species is formed, which makes the latter much more probable. In addition, our analysis reveals that the reverse reactions are comparatively different. In general, the reverse reactions involving NO are found to be less significant than those involving NH by virtue of much lower rate coefficients. For example, if we focus on the formation of NH and NO from N, the rate coefficients of the reverse reactions for NH are orders of magnitude greater than the forward reactions, whereas the rate coefficients of the reverse reactions for NO are orders of magnitude smaller than the forward reactions. We note that reverse reactions for NO are not shown in Figure 6 because their rates are too low. As a result, the steady-state density of NO is much higher than NH.

To date, very few studies of humid-N_2 plasma chemistry have measured gas-phase intermediates,[10,15] and the only modeling effort has focused on gas-surface reactions (i.e., heterogeneous catalysis).[17] For this reason, the main corroboration for our insights are previously reported measurements of fixed nitrogen products. The same trend in NH_3 density (increase in NH_3 density at low RH followed by the constant or slightly decreasing NH_3 density at higher RH) was found by Vervloessem et al. in the gas phase downstream from a plasma jet.[10] In contrast, an earlier work by the same group found that NH_3 trapped as NH_4^+ in a solution downstream of the plasma jet continually increased with RH.[8] Careful spectroscopic measurements showed that NH_3 could be lost downstream of the plasma through reactions with HNO_x.[10] Our work shows that NH_3 loss mechanisms also exist within the plasma itself. Particularly, our model predicts H-abstraction from NH_3 at high RH. Interestingly, this channel is not dominant at low RH where NH_3 loss occurs primarily through direct electron impact dissociation. The latter loss channel is similar to that proposed by Zhang et al. for plasma catalytic conversion of N_2 and H_2O.[38] The impact of NH_3 destruction mechanisms was also discussed by Takahasi and Sasaki, who predicted the loss of NH_3 through its reaction with OH in a low-pressure humid N_2-H_2O inductively coupled plasma by comparing reaction rate constants.[13] While the rate constant of NH_3 reacting with OH is indeed higher than that with H, we have shown that the H density can be considerably higher than OH and therefore the total reaction rate of NH_3 with H is higher. It is important to highlight that our model not only shows the dominant NH_3 loss reaction channels but also, for the first time, shows that they are different at low and high RH.

Similar to our observations, the predominance of NO as compared to NH_3 has been observed by Pattyn et al.[7] and Peng et al.[11] In addition, HNO_2 has been frequently found to be one of the more abundant products in humid-N_2 plasma.[10,60,61] Different trends have been reported, such as the relative amount of NH_3 being higher than NO_x. However, it should be noted that in some cases, the products were measured by capturing and measuring them in liquid.[8] As noted for NH_3, measurements in the gas-phase that are downstream of the plasma may be subject to the chemical instability and continued reactions of the products.[10] In addition, the trapping efficiency of different products is highly dependent on their volatility and solubility and is not truly representative of their gas-phase concentrations. Finally, these studies have involved various plasma sources in terms of power delivery, reactor geometries, gas flow rates, and gas compositions, which lead to different chemistries and necessitates careful consideration when drawing comparisons.[62]

4. CONCLUSIONS

In summary, a simplified low-temperature, atmospheric-pressure plasma system containing systematically controlled mixtures of N_2 and H_2O vapor has been studied to untangle the complex chemistry that is of interest for the sustainable fixation of nitrogen from these readily available feedstocks. Spectroscopic measurements were applied to quantitatively characterize key intermediates. A reaction network was constructed, and a global model was validated by comparing calculations of the densities of the measured species. Based on our results and analysis, we find the following:

1. The generation of N, which is the first step to fixing nitrogen to products such as NH_3, occurs primarily through $N_2(A^3)$ and $N_2(v > 0)$. The lower excitation energy of these species leads to a higher dissociation rate than direct electron impact dissociation of N_2 to produce N.
2. The density of N exhibits a sudden decrease with increasing RH. In comparison, H increases with increasing RH. Thus, NH does not increase with RH, because generation is limited by N, and consumption is enhanced by (reaction with) H.
3. The decrease in N with increasing RH is not because of a competing reaction involving N, but rather because a source of N, $N_2(A^3)$, preferentially reacts with a byproduct of H_2O activation, H_2. The introduction of H_2O is also not found to quench the plasma as T_e remains relatively constant across RH.
4. The byproducts of H_2O activation, H and OH, both react with N, with the former potentially leading to NH_3 and the latter potentially leading to NO_x. Even though the reaction with H has a higher rate, there is a much

https://doi.org/10.1021/acssuschemeng.4c05771
ACS Sustainable Chem. Eng. 2025, 13, 140−150

higher production of NO_x because NH, NH_2, and NH_3 involve multiple steps with kinetically more significant reverse reactions that limit their formation.

This work further highlights the complexity of the chemistry involved in nitrogen fixation via a plasma process. We emphasize that our study focuses on species densities in the plasma, as opposed to downstream or in solution, which has yet to be measured or modeled. A logical extension of this work would be the construction of a 1D or 2D model where transport phenomena, and eventually multiphase systems, could be defined both inside and outside the plasma.

As interest in catalyst-free NH_3 synthesis by plasma processes for sustainable nitrogen fixation grows, the insights that we have obtained into the mechanisms and reaction pathways underlying N_2–H_2O reactivity in a low-temperature plasma help explain many observations in previous reports. In addition, we show that N is a key intermediate for the fixation of nitrogen, and is predominantly formed by excitation of N_2, which is a lower energy pathway than direct electron impact dissociation.[63] Our results could lead to future strategies that tune or optimize the chemistry to increase yield and/or selectivity of desired fixed nitrogen products, or increase the energy efficiency of nitrogen fixation.

■ ASSOCIATED CONTENT

Supporting Information

The Supporting Information is available free of charge at https://pubs.acs.org/doi/10.1021/acssuschemeng.4c05771.

Additional details of plasma characterization including actinometry, LIF/TALIF, and gas and electron temperature measurements, global kinetic model including reaction network, and statistical analysis (PDF)

■ AUTHOR INFORMATION

Corresponding Author

R. Mohan Sankaran − *Department of Nuclear, Plasma, and Radiological Engineering, The Grainger College of Engineering, University of Illinois Urbana−Champaign, Urbana, Illinois 61801, United States;* orcid.org/0000-0002-9399-4790; Email: rmohan@illinois.edu

Authors

Ananthanarasimhan Jayanarasimhan − *Department of Nuclear, Plasma, and Radiological Engineering, The Grainger College of Engineering, University of Illinois Urbana−Champaign, Urbana, Illinois 61801, United States;* orcid.org/0000-0001-7490-9354

Robert Pierrard − *Department of Nuclear, Plasma, and Radiological Engineering, The Grainger College of Engineering, University of Illinois Urbana−Champaign, Urbana, Illinois 61801, United States*

Sean M. Peyres − *Department of Nuclear, Plasma, and Radiological Engineering, The Grainger College of Engineering, University of Illinois Urbana−Champaign, Urbana, Illinois 61801, United States*

Shurik Yatom − *Princeton Plasma Physics Laboratory, Princeton University, Princeton, New Jersey 08543, United States*

Davide Curreli − *Department of Nuclear, Plasma, and Radiological Engineering, The Grainger College of Engineering, University of Illinois Urbana−Champaign, Urbana, Illinois 61801, United States*

Complete contact information is available at: https://pubs.acs.org/10.1021/acssuschemeng.4c05771

Author Contributions

†A.J. and R.P. contributed equally to this work.

Notes

The authors declare no competing financial interest.

■ ACKNOWLEDGMENTS

This material is based upon work supported by the U.S. Department of Energy, Office of Science, Office of Fusion Energy Sciences Plasma Science Frontiers program under award no. DE-SC0023404, and the National Science Foundation ECLIPSE program under award no. 2212110. LIF and TALIF experiments were performed at the Princeton Collaborative Research Facility (PCRF, https://pcrf.princeton.edu), which is supported by the U.S. Department of Energy (DOE) under contract no. DE-AC02-09CH11466.

■ REFERENCES

(1) Ye, D.; Tsang, S. C. E. Prospects and Challenges of Green Ammonia Synthesis. *Nat. Synth* **2023**, *2* (7), 612−623.

(2) Smith, C.; Hill, A. K.; Torrente-Murciano, L. Current and Future Role of Haber−Bosch Ammonia in a Carbon-Free Energy Landscape. *Energy Environ. Sci.* **2020**, *13* (2), 331−344.

(3) Schiffer, Z. J.; Manthiram, K. Electrification and Decarbonization of the Chemical Industry. *Joule* **2017**, *1* (1), 10−14.

(4) Ernst, F. A. *Fixation of Atmospheric Nitrogen*; D. Van Nostrand Company, 1928.

(5) Kogelschatz, U.; Eliasson, B.; Egli, W. From Ozone Generators to Flat Television Screens: History and Future Potential of Dielectric-Barrier Discharges. *Pure Appl. Chem.* **1999**, *71* (10), 1819−1828.

(6) Hawtof, R.; Ghosh, S.; Guarr, E.; Xu, C.; Mohan Sankaran, R.; Renner, J. N. Catalyst-Free, Highly Selective Synthesis of Ammonia from Nitrogen and Water by a Plasma Electrolytic System. *Sci. Adv.* **2019**, *5* (1), No. eaat5778.

(7) Pattyn, C.; Maira, N.; Buddhadasa, M.; Vervloessem, E.; Iseni, S.; Roy, N. C.; Remy, A.; Delplancke, M.-P.; De Geyter, N.; Reniers, F. Disproportionation of Nitrogen Induced by DC Plasma-Driven Electrolysis in a Nitrogen Atmosphere. *Green Chem.* **2022**, *24* (18), 7100−7112.

(8) Gorbanev, Y.; Vervloessem, E.; Nikiforov, A.; Bogaerts, A. Nitrogen Fixation with Water Vapor by Nonequilibrium Plasma: Toward Sustainable Ammonia Production. *ACS Sustainable Chem. Eng.* **2020**, *8* (7), 2996−3004.

(9) Peng, P.; Chen, P.; Addy, M.; Cheng, Y.; Zhang, Y.; Anderson, E.; Zhou, N.; Schiappacasse, C.; Hatzenbeller, R.; Fan, L.; Liu, S.; Chen, D.; Liu, J.; Liu, Y.; Ruan, R. *In Situ* Plasma-Assisted Atmospheric Nitrogen Fixation Using Water and Spray-Type Jet Plasma. *Chem. Commun.* **2018**, *54* (23), 2886−2889.

(10) Vervloessem, E.; Gromov, M.; De Geyter, N.; Bogaerts, A.; Gorbanev, Y.; Nikiforov, A. NH_3 and HNO_x Formation and Loss in Nitrogen Fixation from Air with Water Vapor by Nonequilibrium Plasma. *ACS Sustainable Chem. Eng.* **2023**, *11* (10), 4289−4298.

(11) Peng, P.; Schiappacasse, C.; Zhou, N.; Addy, M.; Cheng, Y.; Zhang, Y.; Anderson, E.; Chen, D.; Wang, Y.; Liu, Y.; Chen, P.; Ruan, R. Plasma *in Situ* Gas−Liquid Nitrogen Fixation Using Concentrated High-Intensity Electric Field. *J. Phys. D: Appl. Phys.* **2019**, *52* (49), 494001.

(12) Sun, J.; Zhou, R.; Hong, J.; Gao, Y.; Qu, Z.; Liu, Z.; Liu, D.; Zhang, T.; Zhou, R.; Ostrikov, K.; Cullen, P.; Lovell, E. C.; Amal, R.; Jalili, A. R. Sustainable Ammonia Production via Nanosecond-Pulsed Plasma Oxidation and Electrocatalytic Reduction. *Applied Catalysis B: Environmental* **2024**, *342*, No. 123426.

(13) Takahashi, J.; Sasaki, K. Production Rates and Destruction Frequencies of Ammonia in Inductively Coupled H_2O/N_2 and H_2/N_2 Plasmas. *Contrib. Plasma Phys.* **2024**, *64* (3), No. e202300167.

(14) Muzammil, I.; Kim, Y.-N.; Kang, H.; Dinh, D. K.; Choi, S.; Jung, C.; Song, Y.-H.; Kim, E.; Kim, J. M.; Lee, D. H. Plasma Catalyst-Integrated System for Ammonia Production from H_2O and N_2 at Atmospheric Pressure. *ACS Energy Lett.* **2021**, *6* (8), 3004−3010.
(15) Sakakura, T.; Murakami, N.; Takatsuji, Y.; Haruyama, T. Nitrogen Fixation in a Plasma/Liquid Interfacial Reaction and Its Switching between Reduction and Oxidation. *J. Phys. Chem. C* **2020**, *124* (17), 9401−9408.
(16) Gromov, M.; Kamarinopoulou, N.; De Geyter, N.; Morent, R.; Snyders, R.; Vlachos, D.; Dimitrakellis, P.; Nikiforov, A. Plasma-Assisted Nitrogen Fixation: The Effect of Water Presence. *Green Chem.* **2022**, *24* (24), 9677−9689.
(17) Hong, J.; Zhang, T.; Zhou, R.; Dou, L.; Zhang, S.; Zhou, R.; Ashford, B.; Shao, T.; Murphy, A. B.; Ostrikov, K.; Cullen, P. J. Green Chemical Pathway of Plasma Synthesis of Ammonia from Nitrogen and Water: A Comparative Kinetic Study with a N_2/H_2 System. *Green Chem.* **2022**, *24* (19), 7458−7468.
(18) Toth, J. R.; Abuyazid, N. H.; Lacks, D. J.; Renner, J. N.; Sankaran, R. M. A Plasma-Water Droplet Reactor for Process-Intensified, Continuous Nitrogen Fixation at Atmospheric Pressure. *ACS Sustainable Chem. Eng.* **2020**, *8* (39), 14845−14854.
(19) Bruggeman, P. J.; Kushner, M. J.; Locke, B. R.; Gardeniers, J. G. E.; Graham, W. G.; Graves, D. B.; Hofman-Caris, R. C. H. M.; Maric, D.; Reid, J. P.; Ceriani, E.; Fernandez Rivas, D.; Foster, J. E.; Garrick, S. C.; Gorbanev, Y.; Hamaguchi, S.; Iza, F.; Jablonowski, H.; Klimova, E.; Kolb, J.; Krcma, F.; Lukes, P.; Machala, Z.; Marinov, I.; Mariotti, D.; Mededovic Thagard, S.; Minakata, D.; Neyts, E. C.; Pawlat, J.; Petrovic, Z. L.; Pflieger, R.; Reuter, S.; Schram, D. C.; Schröter, S.; Shiraiwa, M.; Tarabová, B.; Tsai, P. A.; Verlet, J. R. R.; Von Woedtke, T.; Wilson, K. R.; Yasui, K.; Zvereva, G. Plasma−Liquid Interactions: A Review and Roadmap. *Plasma Sources Sci. Technol.* **2016**, *25* (5), No. 053002.
(20) Bruggeman, P.; Leys, C. Non-Thermal Plasmas in and in Contact with Liquids. *J. Phys. D: Appl. Phys.* **2009**, *42* (5), No. 053001.
(21) Gorbanev, Y.; O'Connell, D.; Chechik, V. Non-Thermal Plasma in Contact with Water: The Origin of Species. *Chem.—Eur. J.* **2016**, *22* (10), 3496−3505.
(22) Sakakura, T.; Uemura, S.; Hino, M.; Kiyomatsu, S.; Takatsuji, Y.; Yamasaki, R.; Morimoto, M.; Haruyama, T. Excitation of H_2O at the Plasma/Water Interface by UV Irradiation for the Elevation of Ammonia Production. *Green Chem.* **2018**, *20* (3), 627−633.
(23) Haruyama, T.; Namise, T.; Shimoshimizu, N.; Uemura, S.; Takatsuji, Y.; Hino, M.; Yamasaki, R.; Kamachi, T.; Kohno, M. Non-Catalyzed One-Step Synthesis of Ammonia from Atmospheric Air and Water. *Green Chem.* **2016**, *18* (16), 4536−4541.
(24) Toth, J. R.; Hawtof, R.; Matthiesen, D.; Renner, J. N.; Sankaran, R. M. On the Non-Faradaic Hydrogen Gas Evolution from Electrolytic Reactions at the Interface of a Cathodic Atmospheric-Pressure Microplasma and Liquid Water Surface. *J. Electrochem. Soc.* **2020**, *167* (11), 116504.
(25) van 't Veer, K.; Engelmann, Y.; Reniers, F.; Bogaerts, A. Plasma-Catalytic Ammonia Synthesis in a DBD Plasma: Role of Micro-discharges and Their Afterglows. *J. Phys. Chem. C* **2020**, *124* (42), 22871−22883.
(26) Niemi, K; Gathen, V S.-v. d.; Dobele, H F Absolute Calibration of Atomic Density Measurements by Laser-Induced Fluorescence Spectroscopy with Two-Photon Excitation. *J. Phys. D: Appl. Phys.* **2001**, *34* (15), 2330.
(27) Yatom, S.; Luo, Y.; Xiong, Q.; Bruggeman, P. J Nanosecond Pulsed Humid Ar Plasma Jet in Air: Shielding, Discharge Characteristics and Atomic Hydrogen Production. *J. Phys. D: Appl. Phys.* **2017**, *50* (41), 415204.
(28) Verreycken, T.; van der Horst, R. M.; Sadeghi, N.; Bruggeman, P. J. Absolute Calibration of OH Density in a Nanosecond Pulsed Plasma Filament in Atmospheric Pressure He−H_2O: Comparison of Independent Calibration Methods. *J. Phys. D: Appl. Phys.* **2013**, *46* (46), 464004.
(29) Yatom, S.; Dobrynin, D. Examination of OH and H_2O_2 Production by Uniform and Non-Uniform Modes of Dielectric Barrier Discharge in He/Air Mixture. *J. Phys. D: Appl. Phys.* **2022**, *55* (48), 485203.
(30) Keniley, S.; Icenhour, C.; Lindsay, A.; Curreli, D.; Panici, D.; Harbour, L.; Schwen, D. Lcpp-Org/Crane: V1.0.0 PSST. *Plasma Sources Sci. Technol.* **2022**, No. 023001.
(31) Keniley, S.; Curreli, D. CRANE: A MOOSE-Based Open Source Tool for Plasma Chemistry Applications. 2019. .
(32) Keniley, S.; Uner, N. B.; Perez, E.; Sankaran, R. M.; Curreli, D. Multiphase Modeling of the DC Plasma−Water Interface: Application to Hydrogen Peroxide Generation with Experimental Validation. *Plasma Sources Sci. Technol.* **2022**, *31* (7), No. 075001.
(33) Giudicelli, G.; Lindsay, A.; Harbour, L.; Icenhour, C.; Li, M.; Hansel, J. E.; German, P.; Behne, P.; Marin, O.; Stogner, R. H.; Miller, J. M.; Schwen, D.; Wang, Y.; Munday, L.; Schunert, S.; Spencer, B. W.; Yushu, D.; Recuero, A.; Prince, Z. M.; Nezdyur, M.; Hu, T.; Miao, Y.; Jung, Y. S.; Matthews, C.; Novak, A.; Langley, B.; Truster, T.; Nobre, N.; Alger, B.; Andrs, D.; Kong, F.; Carlsen, R.; Slaughter, A. E.; Peterson, J. W.; Gaston, D.; Permann, C. 3.0 - MOOSE: Enabling Massively Parallel Multiphysics Simulations. *SoftwareX* **2024**, *26*, No. 101690.
(34) Capitelli, M.; Ferreira, C. M.; Gordiets, B. F.; Osipov, A. I. *Plasma Kinetics in Atmospheric Gases*; Springer Series on Atomic, Optical, and Plasma Physics; Springer Berlin Heidelberg: Berlin, Heidelberg, 2000; Vol. *31*. .
(35) Van Gaens, W.; Bogaerts, A. Corrigendum: Kinetic Modelling for an Atmospheric Pressure Argon Plasma Jet in Humid Air (2013 J. Phys. D: Appl. Phys. 46 275201). *J. Phys. D: Appl. Phys.* **2014**, *47* (7), No. 079502.
(36) Bacri, J.; Medani, A. Electron Diatomic Molecule Weighted Total Cross Section Calculation. *Physica B+C* **1982**, *112* (1), 101−118.
(37) Bahati, E. M.; Jureta, J. J.; Belic, D. S.; Cherkani-Hassani, H.; Abdellahi, M. O.; Defrance, P. Electron Impact Dissociation and Ionization of N_2^+. *J. Phys. B: At. Mol. Opt. Phys.* **2001**, *34* (15), 2963−2973.
(38) Zhang, T.; Zhou, R.; Zhang, S.; Zhou, R.; Ding, J.; Li, F.; Hong, J.; Dou, L.; Shao, T.; Murphy, A. B.; Ostrikov, K.; Cullen, P. J. Sustainable Ammonia Synthesis from Nitrogen and Water by One-Step Plasma Catalysis. *Energy & Environ. Materials* **2023**, *6* (2), No. e12344.
(39) Bang, S.; Snoeckx, R.; Cha, M. S. Kinetic Study for Plasma Assisted Cracking of NH_3: Approaches and Challenges. *J. Phys. Chem. A* **2023**, *127* (5), 1271−1282.
(40) Guerra, V.; Tejero-del-Caz, A.; Pintassilgo, C. D.; Alves, L. L. Modelling N_2−O_2 Plasmas: Volume and Surface Kinetics. *Plasma Sources Sci. Technol.* **2019**, *28* (7), No. 073001.
(41) Tejero-del-Caz, A.; Guerra, V.; Gonçalves, D.; Da Silva, M. L.; Marques, L.; Pinhão, N.; Pintassilgo, C. D.; Alves, L. L. The LisbOn KInetics Boltzmann Solver. *Plasma Sources Sci. Technol.* **2019**, *28* (4), No. 043001.
(42) Voráč, J.; Kusýn, L.; Synek, P. Deducing Rotational Quantum-State Distributions from Overlapping Molecular Spectra. *Rev. Sci. Instrum.* **2019**, *90* (12), 123102.
(43) Voráč, J.; Synek, P.; Potočňáková, L.; Hnilica, J.; Kudrle, V. Batch Processing of Overlapping Molecular Spectra as a Tool for Spatio-Temporal Diagnostics of Power Modulated Microwave Plasma Jet. *Plasma Sources Sci. Technol.* **2017**, *26* (2), No. 025010.
(44) Voráč, J.; Synek, P.; Procházka, V.; Hoder, T. State-by-State Emission Spectra Fitting for Non-Equilibrium Plasmas: OH Spectra of Surface Barrier Discharge at Argon/Water Interface. *J. Phys. D: Appl. Phys.* **2017**, *50* (29), 294002.
(45) Luo, Y.; Lietz, A. M.; Yatom, S.; Kushner, M. J.; Bruggeman, P. J. Plasma Kinetics in a Nanosecond Pulsed Filamentary Discharge Sustained in Ar−H2O and H2O. *J. Phys. D: Appl. Phys.* **2019**, *52* (4), No. 044003.

https://doi.org/10.1021/acssuschemeng.4c05771
ACS Sustainable Chem. Eng. 2025, 13, 140−150

(46) Ono, R.; Teramoto, Y.; Oda, T. Effect of Humidity on Gas Temperature in the Afterglow of Pulsed Positive Corona Discharge. *Plasma Sources Sci. Technol.* **2010**, *19* (1), No. 015009.
(47) Srivastava, N.; Wang, C. Effects of Water Addition on OH Radical Generation and Plasma Properties in an Atmospheric Argon Microwave Plasma Jet. *J. Appl. Phys.* **2011**, *110* (5), No. 053304.
(48) Yu, J.; Zhang, W.; Wu, X.; Wu, L.; Tao, J.; Huang, K. The Influence of Gas Humidity on the Discharge Properties of a Microwave Atmospheric-Pressure Coaxial Plasma Jet. *AIP Advances* **2021**, *11* (2), No. 025131.
(49) Paris, P.; Aints, M.; Laan, M.; Valk, F. Measurement of Intensity Ratio of Nitrogen Bands as a Function of Field Strength. *J. Phys. D: Appl. Phys.* **2004**, *37* (8), 1179.
(50) Paris, P.; Aints, M.; Valk, F.; Plank, T.; Haljaste, A.; Kozlov, K. V.; Wagner, H.-E. Intensity Ratio of Spectral Bands of Nitrogen as a Measure of Electric Field Strength in Plasmas. *J. Phys. D: Appl. Phys.* **2005**, *38* (21), 3894−3899.
(51) Tropina, A.; Shneider, M. N.; Miles, R. B. Nonequilibrium Plasma in Water Vapor. *Plasma Sources Sci. Technol.* **2022**, *31* (11), 114005.
(52) Crofton, M. W.; Welle, R. P.; Janson, S. W.; Cohen, R. B. Temperature, velocity and density studies in the 1 kW ammonia arcjetplume by LIF. *28th Joint Propulsion Conference and Exhibit*; AIAA Aerospace Research Central.
(53) Shin, D. I.; Peiter, G.; Dreier, T.; Volpp, H.-R.; Wolfrum, J. Spatially Resolved Measurements of CN, CH, NH, and H2CO Concentration Profiles in a Domestic Gas Boiler. *Proceedings of the Combustion Institute* **2000**, *28* (1), 319−325.
(54) Schröter, S.; Bredin, J.; Gibson, A. R.; West, A.; Dedrick, J. P.; Wagenaars, E.; Niemi, K.; Gans, T.; O'Connell, D. The Formation of Atomic Oxygen and Hydrogen in Atmospheric Pressure Plasmas Containing Humidity: Picosecond Two-Photon Absorption Laser Induced Fluorescence and Numerical Simulations. *Plasma Sources Sci. Technol.* **2020**, *29* (10), 105001.
(55) Li, L.; Nikiforov, A.; Britun, N.; Snyders, R.; Leys, C. Emission and Absorption Spectroscopy Study of Ar Excited States in 13.56 MHz Argon Plasma Operating at Sub-Atmospheric to Atmospheric Pressure. *Spectrochimica Acta Part B: Atomic Spectroscopy* **2015**, *107*, 75−85.
(56) Teramoto, Y.; Kim, H.-H. Effect of Vibrationally Excited N_2 (v) on Atomic Nitrogen Generation Using Two Consecutive Pulse Corona Discharges under Atmospheric Pressure N_2. *J. Phys. D: Appl. Phys.* **2019**, *52* (49), 494003.
(57) Van Alphen, S.; Vermeiren, V.; Butterworth, T.; Van Den Bekerom, D. C. M.; Van Rooij, G. J.; Bogaerts, A. Power Pulsing To Maximize Vibrational Excitation Efficiency in N_2 Microwave Plasma: A Combined Experimental and Computational Study. *J. Phys. Chem. C* **2020**, *124* (3), 1765−1779.
(58) Vervloessem, E.; Gorbanev, Y.; Nikiforov, A.; De Geyter, N.; Bogaerts, A. Sustainable NO_x Production from Air in Pulsed Plasma: Elucidating the Chemistry behind the Low Energy Consumption. *Green Chem.* **2022**, *24* (2), 916−929.
(59) Miyake, A.; Shirai, N.; Sasaki, K. Contribution of Vibrational Excited Molecular Nitrogen to Ammonia Synthesis Using an Atmospheric-Pressure Plasma Jet. *J. Appl. Phys.* **2024**, *135* (21), 213301.
(60) Pattyn, C.; Maira, N.; Remy, A.; Roy, N. C.; Iseni, S.; Petitjean, D.; Reniers, F. Potential of N_2 /O_2 Atmospheric Pressure Needle-Water DC Microplasmas for Nitrogen Fixation: Nitrite-Free Synthesis of Nitrates. *Phys. Chem. Chem. Phys.* **2020**, *22* (42), 24801−24812.
(61) Janda, M.; Hensel, K.; Tóth, P.; Hassan, M. E.; Machala, Z. The Role of HNO2 in the Generation of Plasma-Activated Water by Air Transient Spark Discharge. *Applied Sciences* **2021**, *11* (15), 7053.
(62) Bogaerts, A.; Centi, G. Plasma Technology for CO2 Conversion: A Personal Perspective on Prospects and Gaps. *Front. Energy Res.* **2020**, *8*, 111.
(63) Wang, W.; Patil, B.; Heijkers, S.; Hessel, V.; Bogaerts, A. Nitrogen Fixation by Gliding Arc Plasma: Better Insight by Chemical Kinetics Modelling. *ChemSusChem* **2017**, *10* (10), 2145−2157.

https://doi.org/10.1021/acssuschemeng.4c05771
ACS Sustainable Chem. Eng. 2025, 13, 140−150